

Complete analytical modeling and analysis of micromachined thermoelectric uncooled IR sensors

C. Escriba*, E. Campo, D. Estève, J.Y. Fourniols

*Laboratory for Analysis and Architecture of Systems (LAAS-CNRS), Research Group, Microsystems and Systems Integration (MIS),
7 Avenue du Colonel Roche, 31077 Toulouse Cedex 4, France*

Received 23 July 2004; received in revised form 22 October 2004; accepted 15 November 2004

Available online 21 January 2005

Abstract

This paper deals with a complete analytical modeling and analysis of thermoelectric uncooled infrared sensors compatible with CMOS technology. The operating principle involves a localized thermal assessment resulting from IR radiation absorption, a micromachined membrane on which PolySi/Al thermojunctions have been deposited causing an internal self-generated electromotive force. The model put forward is based on dividing the sensor into three zones, each one being the subject of a thorough thermal study (conduction, convection and radiation thermal effect). Through the analytical thermal gradient analysis developed in each zone of the structure (absorber, part of thermoelectric transducer layer placed under the absorber, thermoelectric transducer) we are able to predict the sensitivity, detectivity and the noise equivalent power to the sensor. Thus, such a kind of analytical approach is worth of interest to optimize thermopile sensor design parameters.

© 2004 Elsevier B.V. All rights reserved.

Keywords: Infrared thermoelectric sensor; Seebeck effect; Analytical modeling; Optimization

1. Introduction

Advanced technologies allow the massive use of micro-machining devices combined with signal processing to offer complete sensors devices. The aim of this article is to propose the modeling of an infrared CMOS process thermopile in order to optimize low-cost applications, for example, human body detection in domotics. This sensor must operate at room temperature (300 K) with spectral range from 7 to 14 μm , including blackbody reference source for bodies or objects. Respect to the four uncooled solutions: pyroelectric [1], thermoelectric [2], microbolometer [3] and bimaterial microcantilever [4] detection, we focused on thermopile process which allow static human body condition without mechanical systems as required by pyroelectric sensors. As no external supply is needed, no $1/f$ noise could affect the static detection, which is an other good agreement for the

thermopile sensor. The common operating principle relies on the resultant specific area temperature rise of the sensor due to absorption of incident radiations that modify the physical properties of temperature-dependant parameter, such as electrical conductivity. In this study, we first recall the basic equations of thermopiles and we present the structural topology of the sensor under study. Usually, the thermopile optimization models developed are for the majority divided in two zones [5–7], the absorbing layer is separated of the thermoelectric transducer layer. That we would consider the effect in which a part of thermoelectric transducer layer is placed under the absorber to guarantee a good thermal elevation at the hot thermojunction. Thus, we will focus on the model developed in three zones for considering it and analyzing the simulation results. Theses results are derived from the influence of geometric, thermal effects of thermocouples and the absorbing layer relative to the membrane. To do so, we selected a one-dimensional analytical model handling the computational time needed that would be much greater compared at the method of a finite element numerical

* Corresponding author. Tel.: +33 5 61 33 63 60; fax: +33 5 61 33 62 08.
E-mail address: cescriba@laas.fr (C. Escriba).

model. Finally, we will compare some of the simulations obtained from physical coefficients and experimental results to validate our model and underline its merits when it comes to optimizing the performance of thermopile sensors.

2. Thermopile operating principle

Thermoelectrical sensors are based on the use of thermocouples that allow an electromotive force to be generated without any external supply. Fig. 1 shows the connection of two chemically different materials A and B whose ends H (for hot thermojunction) and C (for cold thermojunction) are welded to obtain a circuit. The C point is maintained at a set temperature T_c , while the H point is subjected to incident flow variations Φ_0 (W/m^2) that cause temperature T_h to rise.

Under the effect of differential heating ΔT (K) between the two thermojunctions, a potential difference occurs ΔV_{AB} refer to Seebeck voltage [8,9] that can be expressed as follows:

$$\Delta V_{AB} = \int_{T_c}^{T_h} (\alpha_A - \alpha_B) dT = \alpha_{AB} \Delta T \quad (1)$$

where α_{AB} stands for Seebeck ($\mu\text{V}/\text{K}$) coefficient related to the association of two materials A and B characterized by their respective Seebeck coefficients α_A , α_B and the temper-

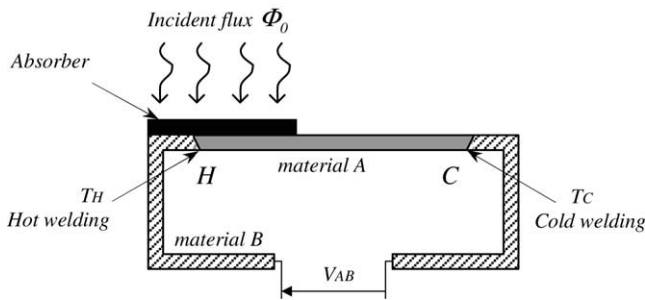
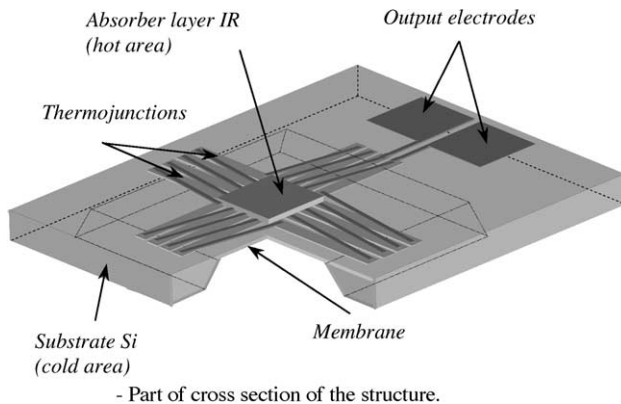


Fig. 1. Seebeck effect principle.



ature difference between the two thermojunctions:

$$\Delta T = T_h - T_c \quad (2)$$

The typical sensor topology selected in this study is shown in Fig. 2. It relies on the association of thermojunctions that have been connected in series so as to increase the voltage delivered. Thus, based on the total number of thermocouples N , the voltage generated by the thermopile can be written as:

$$\Delta V_{AB} = N\alpha_{AB}(T_h - T_c) = N\alpha_{AB}R_{th}\eta P_0 \quad (3)$$

where R_{th} (K/W) is the thermopile's thermal resistance, η the absorption coefficient and P_0 the radiative power (W) collected by the absorbing surface S_a (m^2) of the sensor ($P_0 = \Phi_0 S_a$). Also, to increase the generated voltage, the thermojunctions are deposited on a membrane whose role is to maintain a thermal gradient between both ends of the hot zones subject to absorbed IR radiations and the cold zones maintained at ambient temperature. Thus, the ratio of generated voltage ΔV_{AB} over the power received P_0 stands for the thermopile's electrical sensitivity, denoted \mathfrak{R}_v :

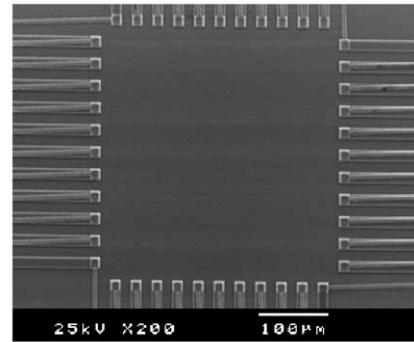
$$\mathfrak{R}_v = \frac{\Delta V_{AB}}{P_0} = N\alpha_{AB}R_{th}\eta \quad (4)$$

3. Thermopile modeling

3.1. Thermal gradient determination

To develop our model, we consider the thermal conduction flows in the materials along the x -axis as well as heat flows exchanged by convection and radiation. Also, as the general structure of the sensor studied exhibits symmetrical axes (Fig. 3a), it is possible to model the whole sensor by means of a single quadrant [10] and to effect the calculation of the thermal gradient ΔT across the ends of thermojunctions using one-dimensional Fourier's stationary heat equations:

$$-\lambda d \frac{\partial^2 T(x)}{\partial x^2} + h(T(x) - T_a) + \sigma_b \varepsilon (T^4(x) - T_a^4) = \eta \Phi_0 \quad (5)$$



- Photomicrograph of the thermojunctions.

Fig. 2. Thermopile's basic structure.

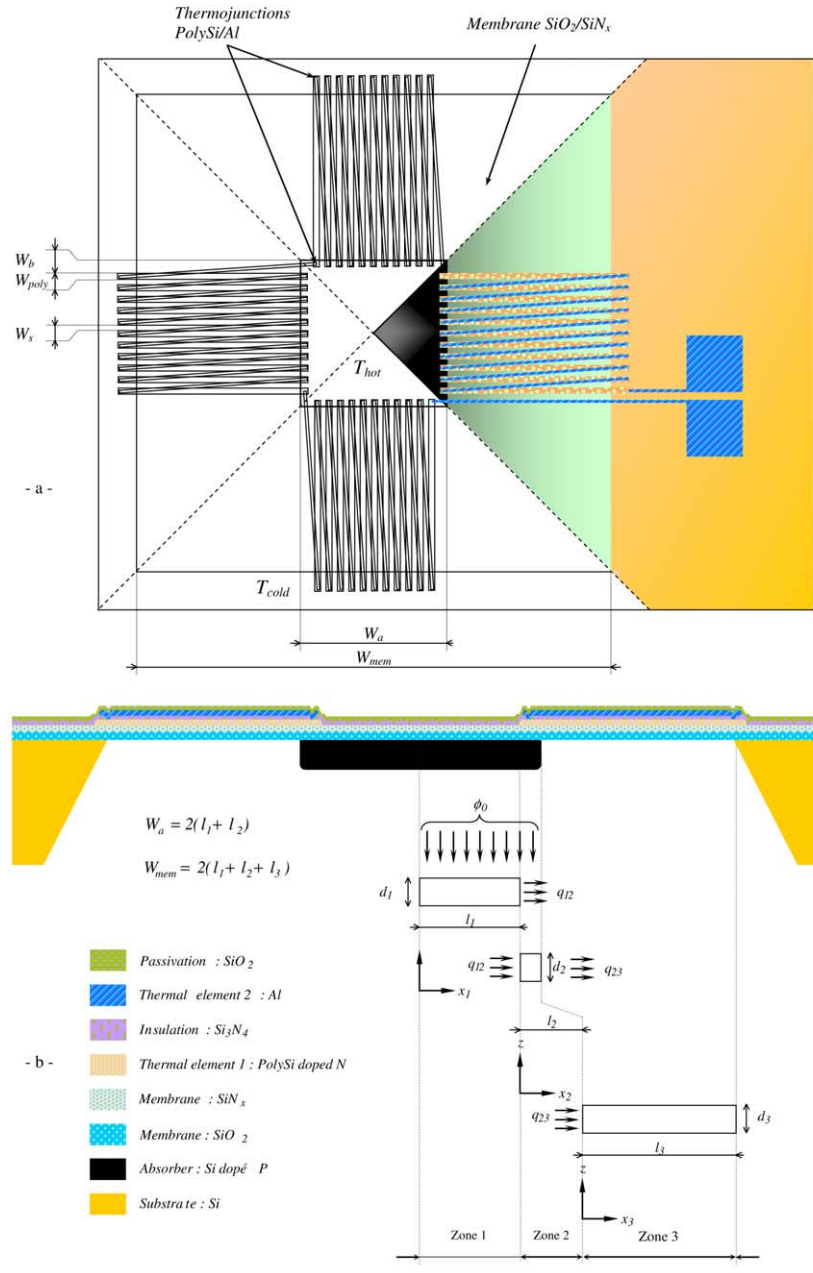


Fig. 3. Overall equivalent diagram.

where λ is the thermal conductivity, d the material thickness, h the convection coefficient, σ_b Stefan-Boltzmann constant, ε the emissivity coefficient and $T(x)$ temperature along the element ∂x .

In addition, the determination of the thermal gradient between the hot and cold thermojunctions, shall be carried out by dividing the overall structure into three zones. Thus, for each zone, the heat transfer equation is computed versus the boundary conditions at each zone's border. Fig. 3b presents the different material layers for each zone, where the terms d_n , l_n , stand for the equivalent thickness and the length of

each zone ($n = 1, 2, 3, 4$) considered along the x axis x_n , with q_{12} and q_{23} the conduction flow at the interface of zones 1–2 and 2–3. Also, considered is the temperature distribution in substrate as a constant and equal to the ambient temperature denoted T_a . Likewise, the thermal gradient in the thickness (z -axis) of each zone shall be disregarded. In other words, if $d_n \ll l_n$, the one-dimensional analytical model will remain valid and the temperature on the front and backsides of the structure shall be the same given the low thickness of membrane [7]. Also, as the temperature difference between the ends of the hot and cold thermojunctions is much smaller

than that of the ambient temperature, one can write the following relationship:

$$\frac{T(x_n) - T_a}{T_a} \ll 1 \tag{6}$$

and

$$T_n(x_n) = T(x_n) - T_a \tag{7}$$

the stationary heat Eq. (5) can be written as a function of Eqs. (6) and (7), with n being the reference index in the zone studied,

$$-\lambda_n \cdot d_n \frac{\partial^2 T_n(x_n)}{\partial x_n^2} + h_n + 4\sigma_b(\varepsilon_{n1} + \varepsilon_{n2})T_a^3 T_n(x_n) = \eta\Phi_0 \tag{8}$$

where λ_n is the equivalent thermal conductivity and d_n the equivalent thickness [10]. Both terms are a function of the number $n' = N/4$ of thermocouples present in the chart and of the thermoelectrical material width, W_{al} for aluminum, W_{poly} for PolySi in the zone under study as well as the absorber width, W_a and of the membrane W_{mem} ε_{n1} and ε_{n2} standing, respectively, for the sensor emissivity coefficient of the front side and back side in the zone n considered:

$$\lambda_n = \frac{\sum_i \lambda_i d_i}{\sum_i d_i} \tag{9}$$

$$d_n = \sum_i d_i \tag{10}$$

with h_n , the convection coefficient [11,12]:

$$h_n = \lambda_g \left(\frac{1}{d_1} + \frac{1}{d_2} \right) \tag{11}$$

where λ_g is the thermal conductivity of the atmospheric gas contained in the box (Fig. 4), d_1 the distance between the membrane and the upper face of the base, d_2 the distance between the membrane and the box cover.

Boundary conditions are as follows: in zone 1,

$$-\lambda_1 \frac{\partial T_1(x_1)}{\partial x_1} \Big|_{x_1=0} = 0 \tag{12}$$

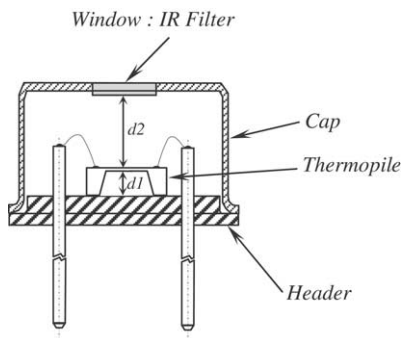


Fig. 4. Cross-sectional view of the encapsulated thermopile.

$$-\lambda_1 \frac{\partial T_1(x_1)}{\partial x_1} \Big|_{x_1=l_1} = q_{12} \tag{13}$$

in zone 2,

$$-\lambda_2 \frac{\partial T_2(x_2)}{\partial x_2} \Big|_{x_2=0} = q_{12} \tag{14}$$

$$-\lambda_2 \frac{\partial T_2(x_2)}{\partial x_2} \Big|_{x_2=l_2} = q_{23} \tag{15}$$

in zone 3,

$$-\lambda_3 \frac{\partial T_3(x_3)}{\partial x_3} \Big|_{x_3=0} = q_{23} \tag{16}$$

$$T_3(x_3)|_{x_3=l_3} = 0 \tag{17}$$

under the boundary conditions (Eqs. (13)–(16)), it appears that the expressions relating to the thermal conduction flow q_{12} , q_{23} are unknown. They are determined after successively solving the differential equations resulting from the thermal elevation $T_n(x_n)$ in each zone n .

The thermal balance in the zone 1, for $0 < x_1 < l_1$ can be as follows:

$$-\lambda_1 d_1 \frac{\partial^2 T_1(x_1)}{\partial x_1^2} dx + A_1 T_1(x_1) = \eta\Phi_0 \tag{18}$$

with A_1 , the coefficient standing for the total loss thermal exchanges at the surface,

$$A_1 = [h_1 + 4\sigma_b(\varepsilon_{11} + \varepsilon_{12})T_a^3] \tag{19}$$

where λ_1 , d_1 , ε_{11} , ε_{12} are the coefficients associated with zone 1, where $T_1(x_1)$ is the thermal elevation along element ∂x_1 . Given the boundary conditions, Eqs. (12) and (13), the thermal elevation of the structure as governed by Eq. (18) in zone 1, can be written as:

$$T_1(x_1) = \frac{\eta\Phi_0}{A_1} - \frac{q_{12}}{\lambda_1 k_1} \frac{\text{ch}(k_1 x_1)}{\text{sh}(k_1 l_1)} \tag{20}$$

with

$$k_1 = \sqrt{\frac{A_1}{\lambda_1 d_1}} \tag{21}$$

The thermal balance in zone 2, for $0 < x_2 < l_2$ can be written as:

$$-\lambda_2 d_2 \frac{\partial^2 T_2(x_2)}{\partial x_2^2} dx + A_2 T_2(x_2) = \eta\Phi_0 \tag{22}$$

with A_2 , the coefficient standing for the total losses of thermal exchanges,

$$A_2 = [h_2 + 4\sigma_b(\varepsilon_{21} + \varepsilon_{22})T_a^3] \tag{23}$$

λ_2 , d_2 , h_2 , ε_{21} , ε_{22} are the coefficients associated with zone 2, where $T_2(x_2)$ stands for the temperature rise along the element ∂x_2 . In accordance with boundary conditions, Eqs.

(14) and (15), the temperature rise of the structure governed by Eq. (22) in zone 2, is of the form:

$$T_2(x_2) = \frac{\eta\Phi_0}{A_2} + \frac{q_{12}}{\lambda_2 k_2} \frac{\text{ch}[k_2(l_2 - x_2)]}{\text{sh}(k_2 l_2)} - \frac{q_{23}}{\lambda_2 k_2} \frac{\text{ch}(k_2 x_2)}{\text{sh}(k_2 l_2)} \quad (24)$$

with

$$k_2 = \sqrt{\frac{A_2}{\lambda_2 d_2}} \quad (25)$$

the thermal balance in zone 3, for $0 < x_3 < l_3$ can be written as:

$$-\lambda_3 d_3 \frac{\partial^2 T_3(x_3)}{\partial x_3^2} dx + A_3 T_3(x_3) = 0 \quad (26)$$

with A_3 , the coefficient standing for the total losses of the surface thermal exchanges,

$$A_3 = [h_3 + 4\sigma_b(\epsilon_{31} + \epsilon_{32})T_a^3] \quad (27)$$

$\lambda_3, d_3, h_3, \epsilon_{31}, \epsilon_{32}$ are the coefficients associated with zone 3, where $T_3(x_3)$ is the temperature rise along the element dx_3 . In accordance with boundary conditions (16) and (17), the temperature rise of the structure governed by Eq. (26) in zone 3, is of the form:

$$T_3(x_3) = \frac{q_{23}}{\lambda_3 k_3} \frac{\text{ch}[k_3(l_3 - x_3)]}{\text{sh}(k_3 l_3)} \quad (28)$$

with

$$k_3 = \sqrt{\frac{A_3}{\lambda_3 d_3}} \quad (29)$$

In Eqs. (20), (24) and (28), conduction flow expressions q_{12}, q_{23} being unknown, a system of equations has to be established by including at the interfaces of zones 1–2 and 2–3, the following conditions:

$$T_1(x_1)|_{x_1=l_1} = T_2(x_2)|_{x_2=0} \quad (30)$$

and

$$T_2(x_2)|_{x_2=l_2} = T_3(x_3)|_{x_3=0} \quad (31)$$

Given Eqs. (30) and (31) and assuming that the material coating of both sides (zones 1 and 2) is of the same nature, the emissivity and convection coefficients are considered identical, that is $\epsilon_{11} = \epsilon_{21}, \epsilon_{12} = \epsilon_{22}$ and $h_1 = h_2$. Hence, the following system of equations:

$$\begin{bmatrix} \frac{\cot h(k_2 l_2)}{\lambda_2 k_2} + \frac{\cot h(k_1 l_1)}{\lambda_1 k_1} & \frac{-1}{\lambda_2 k_2 \text{sh}(k_2 l_2)} \\ \frac{-1}{\lambda_2 k_2 \text{sh}(k_2 l_2)} & \frac{\cot h(k_2 l_2)}{\lambda_2 k_2} + \frac{\text{th}(k_3 l_3)}{\lambda_3 k_3} \end{bmatrix} \begin{bmatrix} q_{12} \\ q_{23} \end{bmatrix} = \begin{bmatrix} 0 \\ \eta\Phi_0 A_2^{-1} \end{bmatrix} \quad (32)$$

Conduction flows q_{12} and q_{23} common to zones 1–2 and 2–3, respectively, can be expressed as:

$$q_{12} = \frac{\eta\Phi_0}{A_2} \xi_{12} \quad (33)$$

$$q_{23} = \frac{\eta\Phi_0}{A_2} \psi_{23} \quad (34)$$

where ξ_{12} and ψ_{12} stand, respectively, for the conduction flow pattern factor:

$$\xi_{12} = \frac{1}{\lambda_2 k_2 [((\cot h(k_2 l_2)/\lambda_2 k_2) + (\cot h(k_1 l_1)/\lambda_1 k_1)) \times ((\cot h(k_2 l_2)/\lambda_2 k_2) + (\text{th}(k_3 l_3)/\lambda_3 k_3)) - (1/\lambda_2^2 k_2^2 \text{sh}^2(k_2 l_2))] \text{sh}(k_2 l_2)} \quad (35)$$

$$\psi_{23} = \frac{(\cot h(k_2 l_2)/\lambda_2 k_2) + (\cot h(k_1 l_1)/\lambda_1 k_1)}{(\cot h(k_2 l_2)/\lambda_2 k_2) + (\cot h(k_1 l_1)/\lambda_1 k_1) \times ((\cot h(k_2 l_2)/\lambda_2 k_2) + (\text{th}(k_3 l_3)/\lambda_3 k_3)) - (1/\lambda_2^2 k_2^2 \text{sh}^2(k_2 l_2))} \quad (36)$$

By introducing the conduction flow expression q_{12}, q_{23} (Eqs. (33) and (34)) in Eqs. (20), (24), (28), we get the analytical expression of the temperature distribution in zones 1, 2 and 3,

$$T_1(x_1) = \eta\Phi_0 \left(\frac{1}{A_1} - \frac{1}{A_2} \frac{\xi_{12}}{\lambda_1 k_1} \frac{\text{ch}(k_1 x_1)}{\text{sh}(k_1 l_1)} \right) \quad (37)$$

$$T_2(x_2) = \frac{\eta\Phi_0}{A_2} \left(1 + \xi_{12} \frac{\text{ch}[k_2(l_2 - x_2)]}{\lambda_2 k_2 \text{sh}(k_2 l_2)} - \psi_{23} \frac{\text{ch}(k_2 x_2)}{\lambda_2 k_2 \text{sh}(k_2 l_2)} \right) \quad (38)$$

$$T_3(x_3) = \frac{\eta\Phi_0}{A_2 \lambda_3 k_3} \psi_{23} \frac{\text{sh}[k_3(l_3 - x_3)]}{\text{ch}(k_3 l_3)} \quad (39)$$

Thus, the thermal gradient expression is computed by establishing the temperature difference between the respective thermocouple ends (Eq. (2)). The hot thermojunction end at T_h is situated under the absorbing layer located in zone 2, at $x_2 = 0$,

$$T_h = T(x_2 = 0) = T_2(x_2 = 0) + T_a = \frac{\eta\Phi_0}{A_2} + \frac{\eta\Phi_0}{A_2} \xi_{12} \frac{\cot h(k_2 l_2)}{\lambda_2 k_2} - \frac{\eta\Phi_0}{A_2} \psi_{23} \frac{1}{\lambda_2 k_2 \text{sh}(k_2 l_2)} + T_a \quad (40)$$

The cold thermojunction is located at the end of zone 3 at $x_3 = l_3$,

$$T_c = T(x_3 = l_3) = T_3(x_3 = l_3) + T_a = T_a \quad (41)$$

Thus, the thermal gradient expression located between T_c and T_h is of the form:

$$\Delta T = \frac{\eta \Phi_0}{A_2} \left(1 + \frac{\xi_{12}}{\lambda_2 k_2} \cot h(k_2 l_2) - \frac{\psi_{23}}{\lambda_2 k_2 \text{sh}(k_2 l_2)} \right) \quad (42)$$

3.2. Sensivity, noise equivalent power, specific detectivity

The thermal gradient expression ΔT being established and taking into account Seebeck coefficients α_1, α_2 , the number of thermocouple for sensor N and the absorption coefficient η are known, the voltage generated by the thermopile (Eq. (3)) subjected to the radiative flow Φ_0 can be written in the following form:

$$V_s = (\alpha_1 - \alpha_2) N \frac{\eta \Phi_0}{A_2} \times \left(1 + \frac{\xi_{12}}{\lambda_2 k_2} \cot h(k_2 l_2) - \frac{\psi_{23}}{\lambda_2 k_2 \text{sh}(k_2 l_2)} \right) \quad (43)$$

The sensor electrical sensitivity (Eq. (4)) can be expressed as:

$$\mathfrak{R}_v = \frac{(\alpha_1 - \alpha_2) N \eta}{A_2 S_a} \left(1 + \frac{\xi_{12}}{\lambda_2 k_2} \cot h(k_2 l_2) - \frac{\psi_{23}}{\lambda_2 k_2 \text{sh}(k_2 l_2)} \right) \quad (44)$$

By identification (Eq. (4)), we get the expression of the thermal resistance R_{th} of the thermopile:

$$R_{th} = \frac{1}{A_2 S_a} \left(1 + \frac{\xi_{12}}{\lambda_2 k_2} \cot h(k_2 l_2) - \frac{\psi_{23}}{\lambda_2 k_2 \text{sh}(k_2 l_2)} \right) \quad (45)$$

By considering that the main source of noise V_n is of a thermal origin (Johnson noise) in this type of sensor [13], the noise equivalent power can be written as follows:

$$NEP = \frac{V_n}{\mathfrak{R}_v} \quad (46)$$

Hence, given the absorbing surface S_a , the noise equivalent power V_n and the Δf , the specific detectivity can be expressed as follows:

$$D^* = \frac{\mathfrak{R}_v \sqrt{S_a \Delta f}}{V_n} \quad (47)$$

4. Discussion on sensor dimensioning

4.1. Analysis methodology

In this study, we have taken into consideration the influence of the absorber, membrane and thermocouples that are a function of l_1, l_2, l_3 and W_{poly} , where l_2 and the thickness of

the different layers in each zone are fixed. We have organized this study in several steps. First, we reviewed the global impact of the polysilicon strip length and width on the whole structure (Fig. 3) to determine a preponderant parameter on sensor sensitivity and thermal gradient between the extremities of thermojunctions. In other words, we customized the absorber dimensions W_a and that of the membrane W_{mem} (Eqs. (48) and (49)) as a function of the thermocouple occupation on the structure (W_s is the space between two thermocouples and W_b the absorber edges).

$$W_a = n' W_{poly} + (n' - 1) W_s + 2 W_b = 2(l_1 + l_2) \quad (48)$$

$$W_{mem} = W_a + 2l_3 \quad (49)$$

Thus, by relying on these first results, we have evaluated the overall influence of the thermocouple dimensions on the sensor's characteristics so as to define the order of magnitude. Then, as above, we evaluated the impact of the absorber and membrane dimensions for a fixed W_{poly} we also reevaluated the impact of the thermocouple dimensions as well as the number of the sensor performance for a fixed absorber surface. This has enabled us to define the optimal size of the membrane and hence that of the thermocouples as well as their number. Finally, the analysis of these results has been compared with a number of experimental values [14–16]. In this modeling, the material thermal values of the Si absorber, SiO₂, SiN_x, PolySi, Al, are 150, 1.4, 1.9, 30 and 235 W/m K, respectively. Likewise, incident flow is 10 $\mu\text{W}/\text{mm}^2$, the emissivity of the absorbing layer $\varepsilon = 0.6$ and electrical resistivity 2 m Ω cm in PolySi and 2.7×10^{-3} m Ω cm in Al, Seebeck coefficient $-110 \mu\text{V}/\text{K}$ for PolySi and $-1.8 \mu\text{V}/\text{K}$ for Al.

4.2. Influence of length and width PolySi strip

In this study, we have customized the dimensions of absorber W_a to the different polysilicon strip widths W_{poly} and to that of the membrane W_{mem} to the length of the thermocouples with $n' = N/4 = 11$ and W_{poly} taking the successive values between 10 and 25 μm in Eq. (48). Simulation shows that the influence of the polysilicon strip on the sensor sensitivity (Fig. 5) for a width W_{poly} in excess of 20 μm is not adequate, for $l_3 = 500 \mu\text{m}$ and $W_{poly} = 25 \mu\text{m}$ the thermal conductance $G_{th} = 123 \times 10^{-6}$ K/W. Nonetheless, this finding is open to question since (Fig. 6) the temperature gradient ΔT between the thermojunction ends is more significant for widths W_{poly} in excess of 20 μm . This finding shows the tradeoff between the sensor sensitivity and the thermal gradient, which is dependent on the one hand, upon the thermal resistance (Eq. (45)) and on the other, on the flow collected at the absorber surface. Indeed, the thermal conductance $G_{th} = 59 \times 10^{-6}$ K/W for $W_{poly} = 15 \mu\text{m}$ of the sensor is much greater for decreasing widths W_{poly} , while the collected flow on the other hand is directly proportional to the absorber surface. Since, W_{poly} modifies the conduction surface of PolySi strips, polysilicon–aluminum total electrical

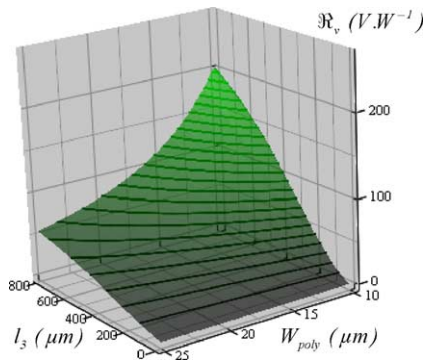


Fig. 5. Sensor response as a function of l_3 and W_{poly} .

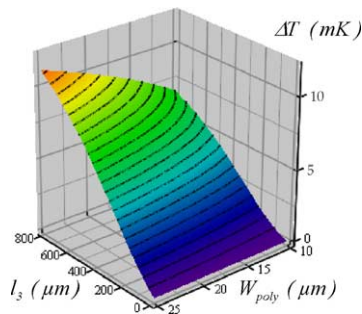


Fig. 6. Thermal gradient between the thermojunctions as a function of l_3 and W_{poly} .

resistance of the thermopile is decreasing with the enlarging PolySi strip. More generally, it is found that it promotes the sensitivity and thermal gradient of the sensor. Nevertheless, as the electrical resistance and NEP (Eq. (46)) of the sensor are antagonistic terms, over-extended thermoelectric strips are not an adequate solution since it would imbalance the tradeoff between sensitivity and detectivity, while mandating the fabrication of a large size membrane. As a result, a good tradeoff between the technological feasibility of a large membrane and the sensor characteristics can be engineered by considering the sensitivity/detectivity issue in terms of thermocouple length.

4.3. Influence of the membrane and absorber dimensions for a fixed size of W_{poly}

In this second study, we review the impact of the size of the absorber W_a and that of the membrane W_{mem} as a function of width W_{poly} set at $15 \mu m$ given the previous results and a number of thermocouples maintained at $n' = N/4 = 11$ in Eq. (48). The simulation shows that the sensor sensitivity (Fig. 7) decreases when the absorber is overdimensioned beyond the transverse space occupied by all the thermocouples, $^*(W_a > n'W_{poly} + (n' - 1)W_s + 2W_b = 2(l_1 + l_2))$.

As stated above, the temperature gradient ΔT between the ends of the thermojunctions (Fig. 8) is more significant owing to the increase in absorber surface. However, despite the thermal gradient increase, it can be noted that the latter

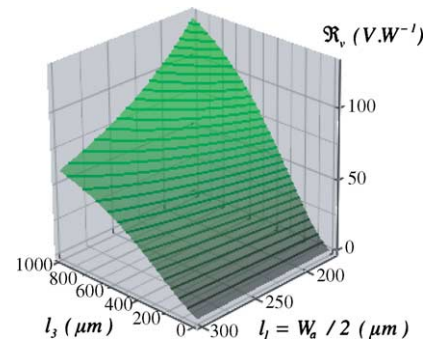


Fig. 7. Sensor sensitivity as a function of l_1 and l_3 .

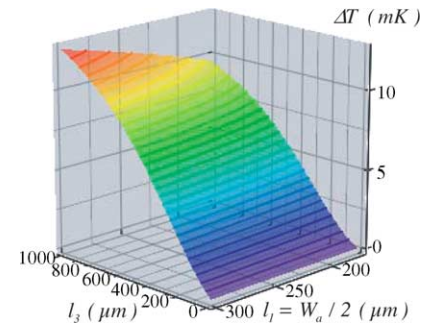


Fig. 8. Thermal gradient between the thermojunctions as a function of l_1 and l_3 .

fails to improve the sensor sensitivity, since the extension of the collected flow absorption surface causes this rise and impacts the thermal resistance. In relative terms we check that the PolySi strip length promotes the sensor sensitivity as well as the thermal gradient. However, it would not be realistic to contemplate possible improvements of the sensor performance by increasing the thermocouple length, since, in addition to the increase in absorber surface which is equally detrimental to the sensor performance (given our working assumptions), we increase the membrane size to no useful purpose. Also, we check that the NEP (Fig. 9) and specific detectivity (Fig. 10) are equally altered. As a result, it follows that there is no use in enlarging the absorber surface, since it is detrimental to the sensor performance as it is higher than the effective* thermocouple occupation.

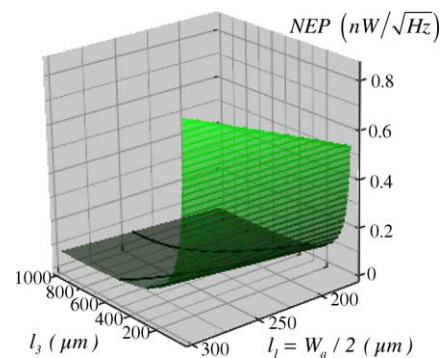


Fig. 9. NEP as a function of l_1 and l_3 .

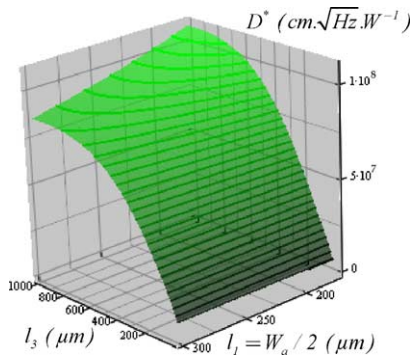


Fig. 10. Specific detectivity as a function of l_1 and l_3 .

4.4. Influence of the number and dimensions of PolySi strips for a fixed size of absorber W_a

To end this study, we intend to re-assess the influence of geometric parameters of the polysilicon strips by setting the absorber size W_a . As a starting assumption, we set $W_{poly} = 15 \mu\text{m}$ and $n' = N/4 = 11$ to evaluate W_a . The calculation yields $W_a = 375 \mu\text{m}$. The absorber size being fixed, we then compute the set of couples $[W_{poly}, N]$ that meet the condition:

$$W_a \approx n' W_{poly} + (n' - 1) W_s + 2W_b = 2(l_1 + l_2)$$

Thus, for each one of the couples determined, the analysis of the results shows that the temperature gradient Δt (Fig. 11) depends primarily on the thermocouple length and that the impact of the couples $[W_{poly}, N]$ is extremely low. This can be accounted for by the notion of equivalent thermal conductivity of the polysilicon strips that we included in our model. Indeed, this last are more or less identical since the disparity of the product N by W_{poly} for each couple is very low. Thus, we conclude that the tradeoff between sensor sensitivity and thermal gradient is associated with the thermocouple length. Therefore, we can fine-tune the sensor performance by selecting a couple $[W_{poly}, N]$ or by increasing the length of the latter. This is why, the sensor sensitivity (Fig. 12) is directly linked to the number of thermocouples and to their length. This finding is highlighted in Figs. 13 and 14 showing the dependence of the sensor sensitivity relative to each cou-

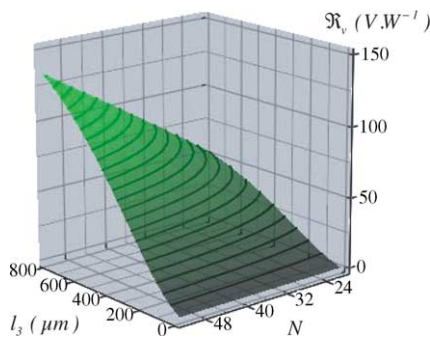


Fig. 11. Thermal gradient between the thermojunctions as a function of $[N, W_{poly}]$ and l_3 .

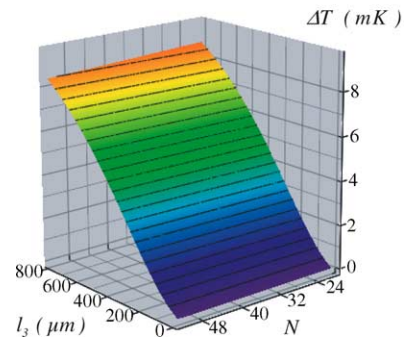


Fig. 12. Sensor sensitivity as a function of $[N, W_{poly}]$ and l_3 .

ple $[W_{poly}, N]$. Nonetheless, it can be seen that the electrical resistance R_{el} of the thermopile depends on the geometric dimensions since in our estimation there is no mention of the equivalent electrical conductivity, only the effective electrical conductivity being considered. This also accounts for the dependence of the noise voltage generated by the thermopile on the real dimensions of thermocouples. This can be seen on curves (Fig. 15) that demonstrate the level of NEP detectable by the sensor. With respect to the specific detectivity D^* the results given in Fig. 16 show that the latter are all the better as thermocouple strips are longer. Therefore, we will remember that for a fixed absorber size, small width thermocouples are preferred, thereby, increasing their number and taking as advantage as much as possible of the Seebeck effect. Finally, only those design rules will impose the optimum size for the thermocouples.

4.5. Comparison with experimental values

To validate our model, we have computed the theoretical sensitivity of thermopiles within the framework of a collaborative effort between LAAS-CNRS and the Univer-

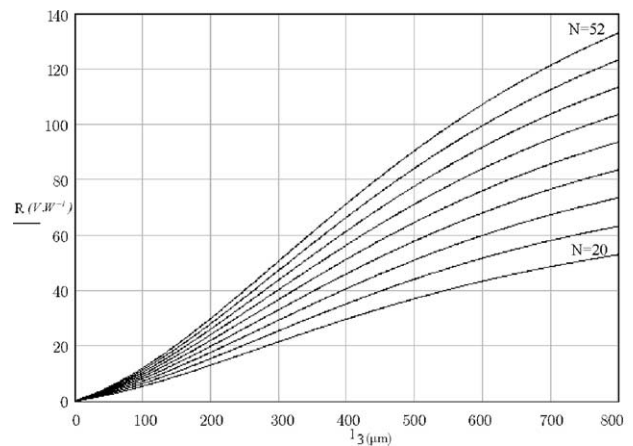


Fig. 13. Sensor sensitivity as a function of W_{poly} and l_3 .

Table 1
Experimental vs. simulated values

Thermopile	Absorber	Membrane	Sensitivity measured (V/W) [17]	Sensitivity simulated (V/W)
TP 09	450 μm × 450 μm	1500 μm × 1500 μm	38 ± 8	40
TP 10	350 μm × 350 μm	1500 μm × 1500 μm	70 ± 14	60
TP 11	600 μm × 600 μm	1500 μm × 1500 μm	21 ± 6	25

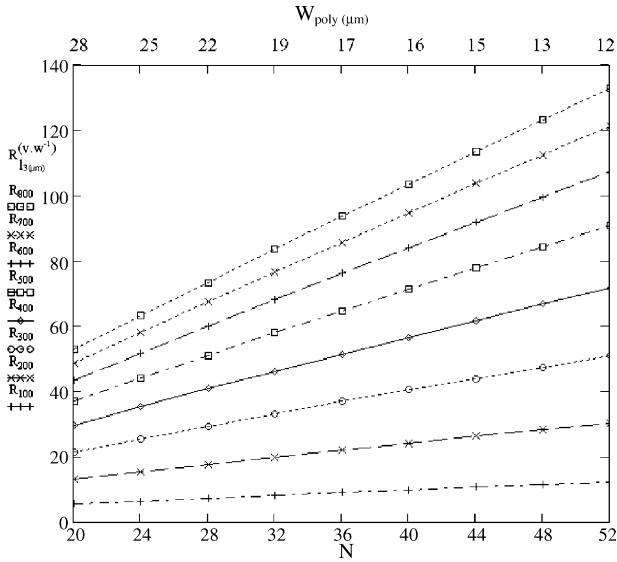


Fig. 14. Sensor sensitivity as a function of $[N, W_{poly}]$ and l_3 .

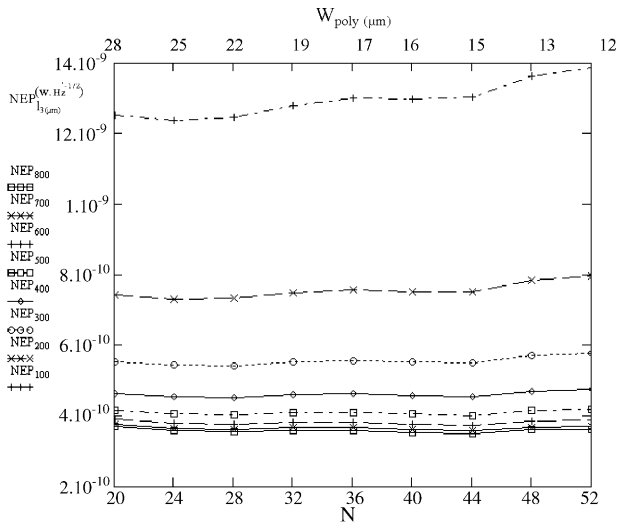


Fig. 15. NEP as a function of $[N, W_{poly}]$ and l_3 .

sity of Barcelona [17]. To do so, we have considered the following characteristics in our model, Seebeck coefficient $\alpha = 96 \text{ V/K}$, the ambient temperature $T_a = 300 \text{ K}$, the incident radiative power at the absorber surface $\Phi_0 = 10 \text{ W/m}^2$, a width $W_{poly} = 25 \text{ μm}$ and the convection coefficient $h = 180 \text{ W/Km}^2$. Thus, Table 1 shows that the theoretical sensitivity obtained from our model are very much like experimental measurement.

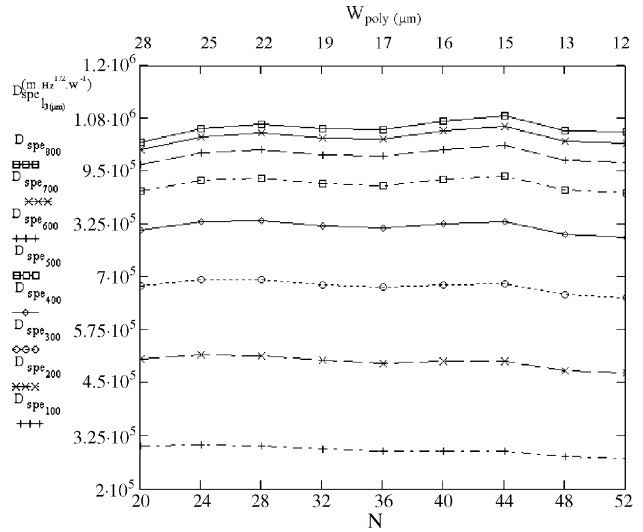


Fig. 16. Specific detectivity as a function of $[N, W_{poly}]$ and l_3 .

5. Conclusion

In this paper, a one-dimensional analytical modeling has been presented with the view of dimensioning an IR thermopile sensor. To do so, we have established the stationary thermal distribution, including phenomena itemized of conduction, convection and radiation along the structure divided into three basic zones. To guarantee a good thermal elevation at the hot thermal junction, we are considered the middle zone in the model, zone where the thermoelectric layer is placed under the absorber. Simulation has supported the prediction of optimal sensor performance by reviewing the impact of the absorber and membrane dimensions, the number and length of thermocouples deposited on the structure. Also, highlighted were the critical parameters for efficient sensors. A preliminary study has shown a good agreement between the simulation and experimental results. A precise metrology of the different topologies of thermopiles fabricated at LAAS-CNRS shall be conducted and compared with the analytical model.

Acknowledgments

This study within the framework of the IMPACT project (*IM*proving *mu*ltidisciplinary *AC*cess to *mi*cro*sy*stems *T*echnologies) supported by the EEC, is conducted by LAAS-CNRS and the University of Barcelona (Electronics Department, Instrumentation and Communication Systems

(SIC)). The project deals with the thermopile sensors study and fabrication dedicated to domotics applications. In particular we would like to thank Drs. M. Moreno, L. Fonseca from CNM for technical discussions and contributions.

References

- [1] B. Ploss, D. Lienhard, F. Sieber, Thermal simulation of micromachined bridges for integrated pyroelectric sensor arrays, *Microelectron. Eng.* 29 (1995) 75–78.
- [2] G.R. Lahiji, K.D. Wise, A batch-fabricated silicon thermopile infrared detector, *IEEE Trans. Electron Devices* 29 (1982) 14–22.
- [3] M. Galeazzi, D. McCammon, Microcalorimeter and bolometer model, *J. Appl. Phys.* 93 (2003) 4856–4869.
- [4] R. Amantea, L.A. Goodman, F.P. Pantuso, D.J. Sauer, M. Varghese, T.S. Villani, L.K. White, Progress toward an uncooled IR imager with 5-mK NETD, *SPIE* (1998) 647–659.
- [5] T. Elbel, R. Lenggenhager, H. Baltes, Model of thermoelectric radiation sensors made by CMOS and micromachining, *Sens. Actuators A35* (1992) 101–106.
- [6] U. Dillner, Thermal modeling of multilayer membranes for sensor applications, *Sens. Actuators A41* (260) (1994) 267.
- [7] A.G. Kozlov, Optimization of thin-film thermoelectric radiation sensor with separate disposition of absorbing layer and comb thermoelectric transducer, *Sens. Actuators A84* (2000) 259–269.
- [8] A.W. Van-Herwaarden, The Seebeck effect in silicon ICs, *Sens. Actuators A6* (1984) 245–254.
- [9] F. Völklein, H. Baltes, Thermoelectric properties of polysilicon films doped with phosphorus and boron, *Sens. Mater.* 3 (1992) 325–334.
- [10] F. Völklein, H. Baltes, Optimization tool for the performance parameters of thermoelectric microsensors, *Sens. Actuators A36* (1993) 65–71.
- [11] D. Chen Hsun, L. Chengkuo, Characterization of thermopile based on complementary metal-oxide-semiconductor (CMOS) materials and post CMOS micromachining, *Jpn. J. Appl. Phys.* 41 (2002) 4340–4345.
- [12] D. Cben Hsun, L. Chengkuo, Optimization criteria of CMOS compatible thermopile sensors, *SPIE* (1999) 116–126.
- [13] E. Socher, O. Degani, Y. Nemirovsky, Optimal design and noise considerations of CMOS compatible IR thermoelectric sensors, *Sens. Actuators A71* (1998) 107–115.
- [14] C. Rossi, P. Temple-Boyer, D. Esteve, Realization and performance of thin SiO₂/SiN_x membrane for microheater applications, *Sens. Actuators A64* (1998) 241–245.
- [15] M. Dumitescu, C. Cobianu, D. Lungu, D. Dascalu, A. Pascu, S. Kolev, A. van-den-Ber, Thermal simulation of surface micromachined polysilicon hot plates of low power consumption, *Sens. Actuators A76* (1999) 51–56.
- [16] J. Schieferdecker, R. Quad, E. Holzenkampfer, M. Schulze, Infrared thermopile sensors with high sensitivity and very low temperature coefficient, *Sens. Actuators A47* (1995) 422–427.
- [17] C. Calaza, M. Moreno, S. Marco, L. Fonseca, C. Cané, L. Gràcia, J.Y. Fourniols, G. Soto-Romero, F. Bony, Design fabrication and characterisation of CMOS compatible thermoelectric IR sensors for gas analysis application, 7th Int. Conf. IR Sens. Systems, 2002, p. 6.

Biographies

C. Escriba received the Master's degree in Conception of Microelectronics and Microsystems Circuits from the Polytechnic National Institute ENSEEIHT (Ecole Nationale Supérieure d'Electrotechnique, d'Electronique, d'Informatique, d'Hydraulique et des Télécommunications) of Toulouse (France) in 2001. He is preparing a PhD thesis in microelectronics at the LAAS-CNRS, working on the realization of micromachined uncooled Infra Red thermal sensors.

E. Campo is an Assistant Professor at Toulouse II-Blagnac I.U.T (University Institute of Technology), since 1994. He obtained his PhD in Electronics from the INSA (National Institute of Applied Sciences) at Toulouse in 1993. He has been conducting research at LAAS-CNRS and belongs to ICARE research team from IUT-Blagnac engaged in wireless communicating microsystems and systems. He is primarily involved in home automation field where he has coordinated a number of multidisciplinary projects dedicated to monitoring the elderly at home and to the comfort management. The applications of the wireless systems developed concern now also civil engineering, aeronautics or aquatic fields.

D. Estève is Research Director at CNRS. He joined the LAAS in 1966 to work in the domain of electronics components and integrated circuits. Between 1977 and 1997 he was deputy director of LAAS. Initially, specialized in microelectronics issues, he focused on microsystems and their application as early as the eighties. He is one of the promoters of microtechnologies and microsystems in France and even in Europe. He is the coordinator of the smart home center at CNRS/SPI. His current research interests are microsystems integration and inclusion of larger systems based on communicating microsystems.

J.Y. Fourniols is French Engineer in Electronics Automatics and Computer Design (1993). He obtained his PhD in 1996, and was a space design engineer in MATRA MARCONI SPACE from 1993 to 1997. He works on ATV program and develops docking procedures with differential GPS techniques. He is, since September 1997, an Assistant Professor at National Institute of Applied Sciences at Toulouse. He makes his research at LAAS and his interests includes development of Microsystems principally dedicated to space applications: micro-camera design, micro Infra Red Earth sensors development, Infra Red sensors and systems development, accelerometers systems and MEMS reliability characterization. He is now involved as a technical microsystems specialist in the reliability program of the CNRS.